Journal of Electronic Materials (2023) 52:5039–5046
https://doi.org/10.1007/s11664-023-10272-6

TOPICAL COLLECTION: 19TH CONFERENCE ON DEFECTS (DRIP XIX)

Extended Defects in SiC: Selective Etching and Raman Study

J. L. Weyher[1] · A. Tiberj[2] · G. Nowak[1] · J. C. Culbertson[3] · J. A. Freitas Jr.[3]

Received: 17 October 2022 / Accepted: 20 January 2023 / Published online: 8 February 2023
© The Author(s) 2023

Abstract
Controlling the electrical properties of SiC requires knowledge of the nature and properties of extended defects. We have employed orthodox defect-selective etching and photo-etching methods to reveal typical and new structural defects in commercial SiC wafers. For photo-etching, the etch rate increases as the free carrier concentration decreases. The etch rate can be used to estimate the free carrier concentration with higher precision, and over a larger lateral and depth range than that accessed by Raman scattering. The logarithmic dependence of the etch rate on the free carrier concentration has been characterized.

Keywords Defect-selective etching · silicon carbide · Raman spectroscopy · micro-pipes · dislocations · biaxial stress · optical phonons

Introduction

Knowledge of material defects is essential to improve material quality and device performance. Wet chemistry in the form of preferential etches is an important tool for the study of defects and device fabrication. Preferential etches have been developed to reveal extended defects which are difficult to detect by other techniques.

Different types of defects, such as dislocations, stacking faults (polytype inclusions), second phase inclusions, voids, surface pits, and micro-pipes (MPs) are nucleated in SiC substrates and epitaxial layers.[1–7] The influence of defects on the properties of epitaxial layers and on the performance of subsequently manufactured electronic devices has been thoroughly investigated,[8–11] but there remains a constant need to reveal defects, identify their nature, and verify their effects.

Molten bases, transmission electron microcopy, and x-ray topography are frequently used for studying crystallographic defects (see, e.g.,[1–6,12,13]), while spectroscopic techniques are commonly used for analysis of electrical properties of bulk SiC single crystals and epitaxial layers.[7,9–11,14,15] The advantage of revealing defects, such as dislocations and stacking faults in SiC, using shallow open-circuit photo-etching, has also been demonstrated.[16,17]

Galvanic and electroless photo-etching methods have been effectively employed to reveal and provide a quantitative analysis of crystallographic and electrically active defects in III–V compound semiconductors.[18,19] By direct calibration of photo-etching methods with electron beam-induced current (EBIC) measurements and Raman spectroscopy, the relationship between the photo-etch rate and carrier concentration was established for GaAs and GaN single crystals,[20,21] introducing a quantitative analysis of extended defects and inhomogeneous properties of these semiconductors. Finally, the ultra-high sensitivity of the photo-etching method was demonstrated by clearly revealing growth striations induced by Marangoni convection in space-grown GaAs single crystals, while the EBIC method used on the same material failed to measure any changes in carrier concentration across these non-homogeneities.[22]

In the present paper, photo-etching of SiC crystals in KOH solutions and in its modified version, named KSO-D ($KOH + K_2S_2O_8$[23]), has been used to reveal and identify electrically active extended/structural defects. The presence

J. L. Weyher
weyher@unipress.waw.pl

J. A. Freitas Jr.
jaime.freitas@nrl.navy.mil

1 Institute of High Pressure Physics, Polish Academy of Sciences, Ul. Sokolowska 29/37, 01-142 Warsaw, Poland

2 Laboratoire Charles Coulomb, Université Montpellier II, Place Eugène Bataillon, 34095 Montpellier, France

3 Naval Research Laboratory, Electronics Science & Technology Division, Washington, DC 203755321, USA

of peculiar types of hexagonal-shaped planar defects, as well as extended and fine-scale growth striations, have been highlighted/presented. To establish the properties of these complex non-homogeneities, the etched samples were probed by micro-Raman scattering spectroscopy (μRS) to obtain insights into variations in free carrier concentration and stress.

Experimental

Two-inch (c. 5-cm) diameter *n*-type well-oriented (0001) 4H-SiC wafers with nominal carrier concentration ~ 6.8×10^{18} cm^{-3} were cut into 5 × 10 mm samples. Two photo-etching systems were used to reveal defects: (1) 0.1 M KOH solution as in Ref. 16 and (2) KSO-D etch previously developed for revealing defects in GaN,[23] modified for 4H-SiC treatment (0.2 M KOH + 0.1 M $K_2S_2O_8$), which will subsequently be called the KOH-KSO etch. Etching was performed using illumination from a 300-W UV-enhanced Xe lamp (Oriel). Ti contacts sputtered on part of the SiC sample surface were used in the KOH solution etching (galvanic etching method), while KOH-KSO solution etching was on samples without evaporated Ti contact, but with Ti springs touching the etched SiC surface. Wax spots were placed on the sample surfaces to measure the etch rate. The etching depth profiles were recorded using a Tencore Alfa step profiler and an NTegra atomic force microscope (AFM). A third etch, the molten KOH + NaOH eutectic solution with 10% of MgO (E + M etch[24]), was used to reveal dislocations.

The etched samples were investigated by two room-temperature micro-Raman spectrometers. The first (μRS-1) was a Jobin Yvon-Horiba T64000 spectrometer in the confocal mode, with 100 × microscope objective. The 514 nm line of an Ar ion-laser was used for excitation with a spot size of ~ 1 μm and a power of 1 mW under the objective. An XYZ piezo-stage was used to acquire Raman mapping and Raman profiles on the same area probed either by optical microscopy or by a step profiler.

The second micro-Raman spectrometer (μRS-2), employed to acquire longitudinal and transverse phonon Raman spectral images, was a co-axial micro-Raman system consisting of a single-mode 488-nm laser, a half-meter Acton spectrometer with an 1800rgroove/mm holographic grating, and a Princeton Instruments back-thinned, deep depleted, nitrogen-cooled CCD (1340 × 400 pixel array). The spectral resolution of this configuration of the system was 2.5 cm^{-1}, and the repeatability with which a line position can be determined was within 0.1 cm^{-1}. The laser power was attenuated using neutral density filters. Sample excitation with the 488-nm laser was made co-axial with the detection axis using a SEMRock dichroic beam splitter. The laser was focused, and the Raman collected using a ×50 Mitutoyo microscope objective lens having a numerical aperture of 0.65, yielding a spot size on the order of 360 nm. Two SEMRock long-pass filters were placed in front of the spectrometer to filter out the laser light. Samples were mounted on a precision, computer-controlled Aerotech XYZ translator having a bi-directional position accuracy of better than 0.1 μm. Raman spectra and the incident laser power were measured and stored for each position in each spatial map.

The hexagonal SiC polytypes belonging to the space group $C_{6v}{}^4$ have *n*(H) atoms in their unit cells, where H stands for a hexagonal bi-layer of Si and C atoms. The 4H polytype, discussed in the present work, has 8 atoms in its unit cell. The axial modes (atomic displacements parallel to the crystal *c*-axis, corresponding to the (111) direction of the zinc blende structure) consist of Raman active A_1 and Raman inactive B_1 modes, while the planar modes (atomic displacements perpendicular to the crystal *c*-axis) consists of Raman and infrared active E_1 modes and Raman active E_2 modes. The unit cell length of each hexagonal polytype, along the *c*-axis, is *n*-times larger than that of the basic cubic (3-C) polytype. The stacking arrangement of these polytypes introduces an ordering, reducing the basic Brillouin zone in the Γ-L direction by $1/n$. As a consequence, the dispersion curves of the phonons are folded, which allows the observation of the acoustic phonons at the center of the Brillouin zone, where the Raman scattering spectra are detected. This becomes handy for the identification of the polytypes and stacking faults imbedded in the bulk of the crystals. All of the first-order allowed phonons have been previously observed.[25] All first-order phonons are observed in our samples, namely: A_1 longitudinal acoustic mode at 611 cm^{-1}, the two TO modes at 778.5 cm^{-1} (E_2 symmetry) and 798.9 cm^{-1} (E_1 symmetry), and the A_1 (LO) phonon at 964 cm^{-1}. Also observed (in the range 980 cm^{-1}–1015 cm^{-1}) is the LO phonon–plasmon coupled mode (LOPC mode) resulting from the interaction between the collective excitation of free carrier (plasmon) and the pure longitudinal optical mode (GaAs)].[26] The Raman peak position and line shape of the LOPC mode are strongly sensitive to the free carrier concentration and are conveniently used in this study to estimate the free carrier concentration across our samples.

Results and Discussion

Figure 1a shows an optical microscope image of planar defects revealed by shallow KOH photo-etching of *n*-type SiC; the etch depth of the perfect SiC matrix was 100 nm. These defects are not observed on polished surfaces before etching. Some hexagonal defects, such as the one indicated by the arrow, show complex morphology. A magnified view of the boundary of this non-homogeneously etched area is shown in Fig. 1b. The etch depth profile along the y–y' line

is highlighted in Fig. 2a, and the corresponding profile of carrier concentration estimated from Raman measurements is represented in Fig. 2b. The increased etch rate corresponds to lower carrier concentration, as was observed previously for GaAs[20] and GaN.[21]

Apart from the hexagonal shaped non-homogeneities, relatively long straight line defects (indicated by the arrow), depicted in Fig. 3a, were revealed by the photo-etching. Surface profiling of one of these lines, highlighted in Fig. 3b, showed that these lines are ridges with variable etch rates across them. Raman measurements (μRS-1) carried out along the x–x' line, represented in Fig. 3c, confirmed that lower etch rates correspond to the increased carrier concentration. The "characteristic" of this gross defect (size, shape, carrier distribution, and etching behavior) lead to the conclusion that this defect is a growth striation (for comparison, see, e.g., defects revealed by photo-etching in GaAs[20]). A summary of the measurements of carrier concentration related to the etch rate of both the hexagonal defects and the growth striation, acquired from different SiC wafers, are summarized

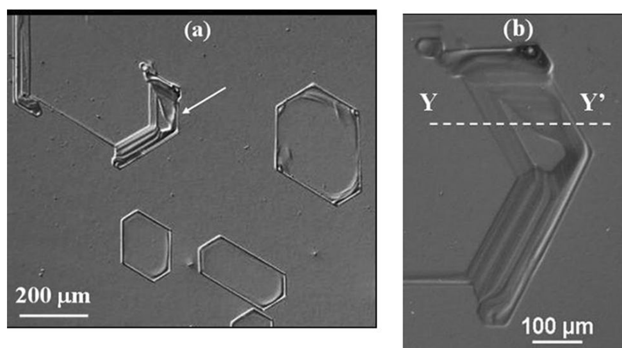

Fig. 1 Differential interference contrast (DIC/Nomarski) optical image of Si-surface of n-type SiC crystal after shallow photo-etching in a KOH solution: (a) different hexagonal shape defects; a magnified fragment of the defect boundary indicated by the arrow in (a) is shown in (b).

in Fig. 4. Surprisingly, all the measurements of carrier concentration versus the etch rate performed on different samples fit well to a single line, as shown in Fig. 4b. Such an experimental result remains in contradiction to previously reported results for GaAs and GaN,[20,21] where the relationship between etch rate (R) and carrier concentration (n) (R = f log(n) curve) of each sample showed a parallel shift. This observed discrepancy in SiC samples with similar average carrier concentration is most likely related to the relatively small ratio of surface area of non-homogeneities versus the whole surface of the etched sample, while, in the previously examined GaN crystals, this ratio was in the range of tens of percent and was different in the two examined samples.[21] This conclusion on the role of the percentage of areas with large carrier concentration differences on the shift of R = f log(n) curves was explained in Ref. 27

A new gross defect characterized by a quadrupole pattern of striations (QPS), seen at the bottom of Fig. 5, is revealed by shallow electroless photo-etching (etch depth ~ 65 nm, in KOH-KSO solution for 10 min) of SiC samples. As a rule, the quadrupole patterns are situated close to complex defects, such as outcrops of micro-pipes (MPs), that have dislocation half-loops pinned on them. These are basal plane dislocations (BPDs; D); ridges form along them during photo-etching, as shown in Fig. 5. It seems, however, that the QPS are independent of the existence and density of the BPDs, while the vicinity of MPs was always confirmed. It should be noted that: (1) emanation of half-loops of prismatic and BPDs from MPs was explained based on synchrotron x-ray topography (see Fig. S1, after Ref 28 .) and some illustrative examples of the MP + D complex defect revealed in different SiC samples are presented in Fig. S2, and (2) the presence of inclusions in the MPs cannot be excluded. However, penetration of orthodox etching medium (molten E + M etch) placed on the Si-face and local dissolution of the back C-face of etched samples proves that the MPs form empty tubes. In addition, examination of both two-sides-polished and

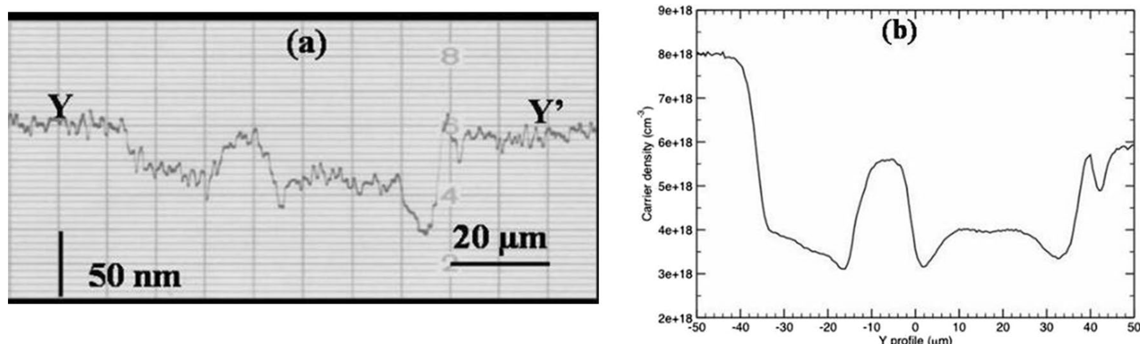

Fig. 2 (a) Surface profile of etch depth along the y–y' line from Fig. 1b after shallow photo-etching in a KOH solution; (b) carrier concentration profile along the same y–y' line obtained from Raman measurements (μRS-1).

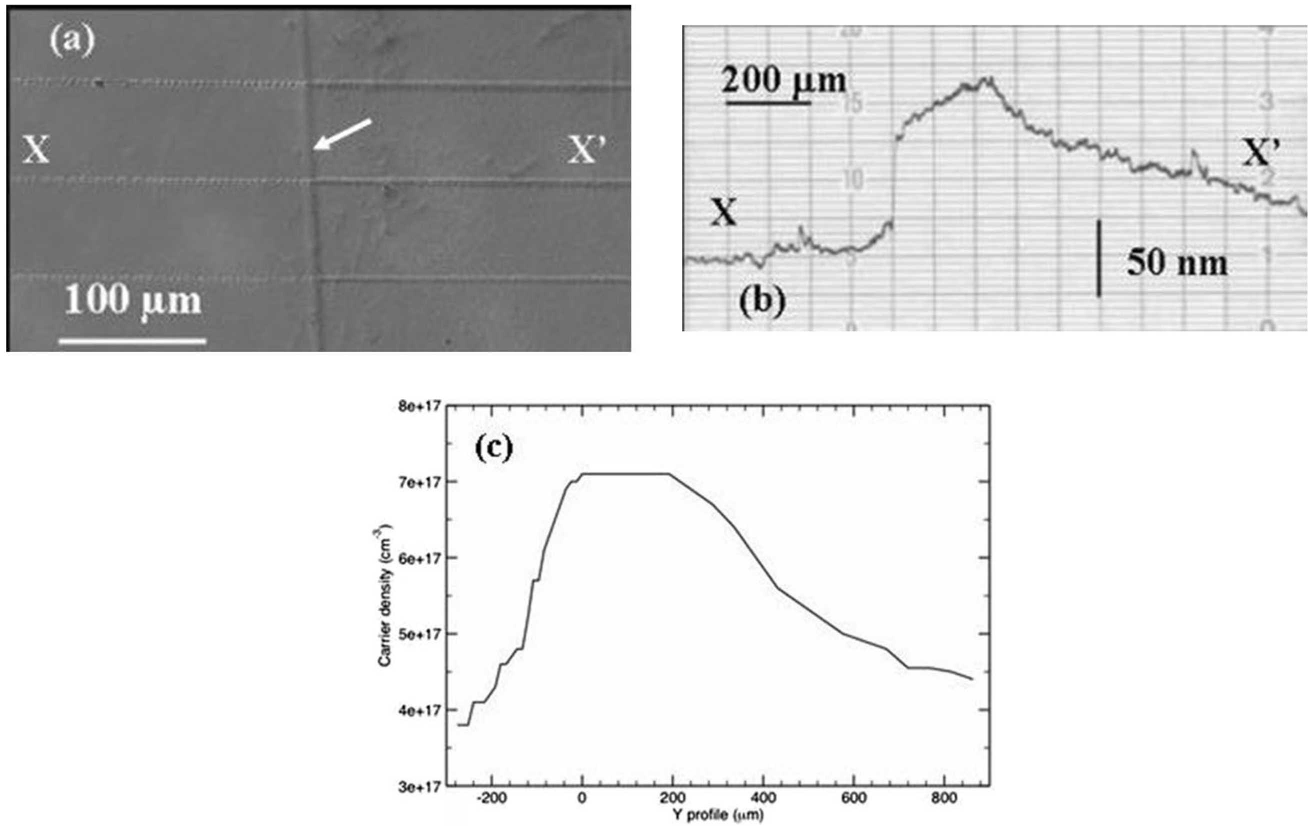

Fig. 3 (a) Differential interference contrast (DIC/Nomarski) optical image of linear defect (vertical line) revealed by KOH photo-etching (three traces of surface profiling are visible); (b) surface depth and (c) carrier concentration profiles (from Raman scattering, μRS-1), measured along the x–x' line.

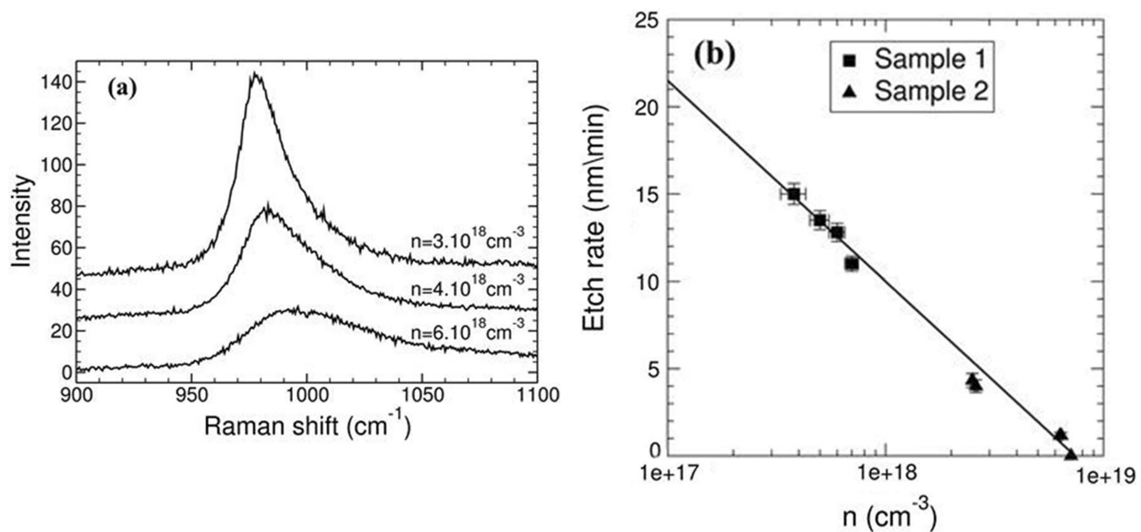

Fig. 4 KOH etch rate versus free-carrier concentration: (a) Raman spectra (μRS-1) of the LOPC mode measured at three points on the etched samples that correspond to three different carrier densities; (b) relationship between the logarithm of the free carrier concentration n (determined from Raman spectroscopy) and the etch rate R for the KOH etch. The equation of the linear fitting is: $R = -11.5 \log(n) + 217$. Sample 1 (see Fig. 3(a–c)) and Sample 2 (see Figs. 1(b) and 2(b)).

one-side-polished and photo-etched samples proves that MPs form via-tubes (see Fig. S3 and Fig. S4, respectively).

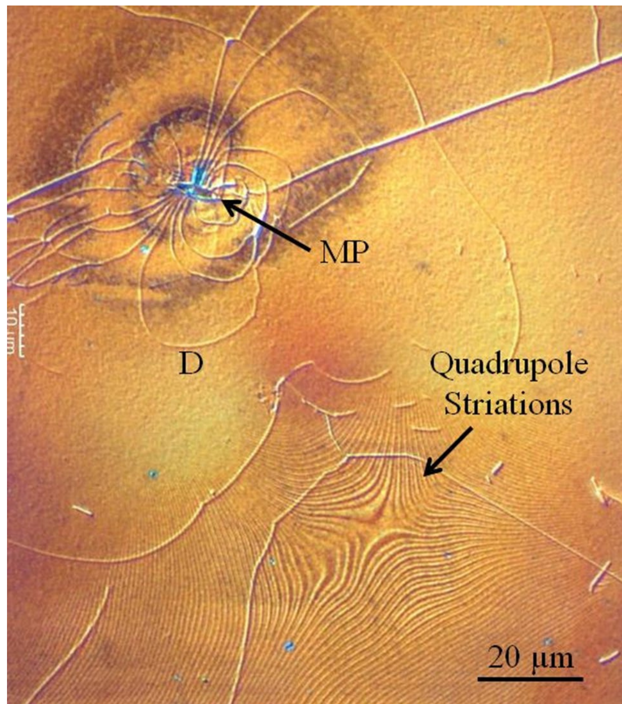

Fig. 5 Defects revealed by shallow KOH-KSO photo-etching in *n*-type SiC sample; differential interference contrast (DIC/Nomarski) image.

Figure 6 shows a part of the quadrupole striation defect from Fig. 5 as viewed by (a) optical microscopy and (b) AFM. These quadrupole striations are not detectable in high spatial resolution Raman measurements using the free carrier-sensitive LOPC phonon line or the strain-sensitive E_2 phonon line. These surface relief striations were made visible due to the different etch rates existing for the bands of material that make up the striations. Because MPs and screw-type dislocations constitute effective sources of growth steps, large hillocks are formed around these defects during vapor-phase growth.[29–32] The lapped and polished surface of the SiC wafer intersects the non-planar growth front. Subsequent photo-etching reveals changes in the composition of the vapor phase before the growth front, which appears as growth striations. Figure 6c shows a surface profile measured across the striations seen in the AFM measurement and shown in Fig. 6b. The difference in the etch rate between ridges and valleys across these striations (average etch depth p ~ 65 nm, Δp ~ 7 nm, V_e max ~ 7.2 nm/min and V_e min ~ 6.5 nm/min) allows estimation from Fig. 4b that the corresponding carrier concentrations are 6×10^{18} and 6.88×10^{18} cm^{-3}, respectively. This result confirms the photo-etching method of detecting very small differences in electrical properties of *n*-type SiC is more sensitive than measurements of the Raman free carrier-sensitive LOPC line.

Apart from isolated hexagonal defects shown in Fig. 1a, large hexagonal-shaped defects are frequently observed around MPs. A typical example of such a complex defect is shown in Fig. 7a. The photo-etch rate of four overlapped

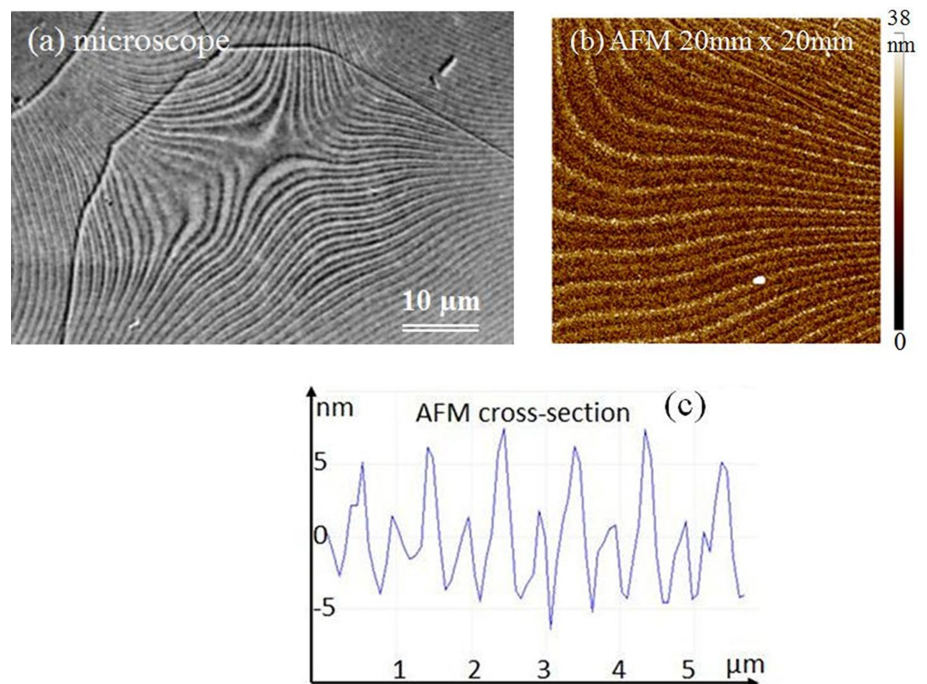

Fig. 6 A KOH-KSO etch-revealed feature of the quadrupole-striation defect shown in Fig. 5. Post-etch, these striations are seen as surface-topography, optically visible (a) in this differential interference contrast (DIC/Nomarski) optical image and measurable in detail using AFM (b). (c) A bimodal height profile measured from (b); combining this with the etch rate dependence on free-carrier density, one can infer the magnitude of the charge oscillations responsible for these bands.

hexagons is variable and slightly larger than the etch rate of the surrounding defect-free matrix. The estimated carrier concentration from Raman measurements (μRS-1) at different positions (1–5 as shown in Fig. 7a) confirmed the relationship indicated in Fig. 4b; the hexagons with lower carrier concentration are etched at a higher rate as compared to the matrix. Figure 7b shows the same defect as Fig. 7a, after an additional etch was carried out to create etch-pits at the surface termini of threading dislocations. There is no apparent association between the four superimposed hexagons and the locations of the etch-pits. Figure 8 shows Raman maps (μRS-2) of the Raman shift of the free carrier-sensitive LOPC mode (a) and the strain sensitive E_2^2 phonon (b) for the same defect shown in Fig. 7. The isolated spots on Fig. 8b correspond to the locations of the etch-pits seen in Fig. 7b. These etch-pits are not detectable in the free carrier-sensitive Raman map shown in Fig. 8a.

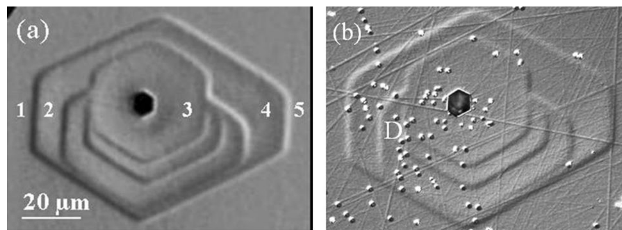

Fig. 7 Differential interference contrast (DIC/Nomarski) optical images of hexagonal defects formed around a micro-pipe and revealed by KOH photo-etching (a) and subsequent orthodox etching in molten (E + M) etch (b). Carrier concentrations from Raman LOPC mode at positions: (*1*) $n = 4.5 \times 10^{18}$, (*2*) $n = 3.7 \times 10^{18}$, (*3*) $n = 3.3 \times 10^{18}$, (*4*) $n = 3.4 \times 10^{18}$, (*5*) $n = 4.4 \times 10^{18}$ cm^{-3}.

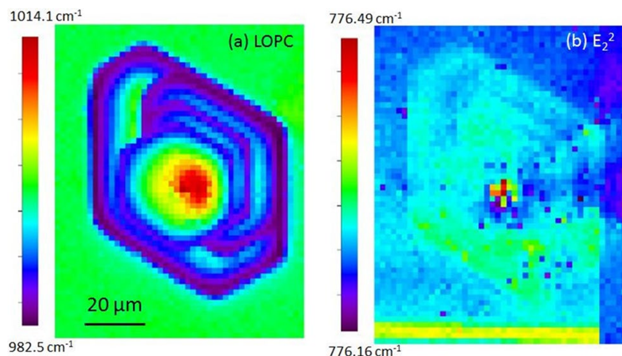

Fig. 8 Raman spectra (μRS-2) were measured at 2-*μ*m intervals over a 90 *μ*m × 114 *μ*m region containing a four-hexagon defect in 4H-SiC. Spatial maps are shown for the Raman shift of the (a) LOPC mode and the (b) E_2^2 phonon. The Raman shift of the LOPC mode increases with increasing free carrier concentration. The Raman shift of the E_2^2 phonon shifts with stress. The small etch pits that decorate screw/edge dislocations do not show up in the free carrier concentration map (a), but do show up in the stress map (b). Note the region of highest free carrier concentration is at the middle of this four-hexagon defect.

Raman maps (μRS-2) of a simple hexagonal defect are shown in Fig. 9. Figure 9a shows a map of the Raman-shift of the LOPC mode, which increases with increasing free carrier concentration. Figure 9b shows a map of the Raman shift of the E2 phonon which increases with increasing compressive stress. Relative to the material surrounding the hexagonal defect, the free carrier concentration on the border of the defect is depressed, while the free carrier concentration within the defect tends to be higher. The results of photo-etching and Raman measurements clearly show the well-defined morphology of these planar defects and their electrical properties. However, the mechanism of formation of these defects remains unclear. Although the dimensions and shape of planar defects are similar to the hexagonal voids or so-called planars,[33,34] the non-homogeneities shown in Figs. 1a and 7a have different natures. It seems that these defects are formed due to non-uniform incorporation of dopants or impurities, as was recently suggested from the abnormal behavior of the LOPC mode recorded in the hexagonal defects.[14] It should be mentioned that none of the hexagonal defects revealed by photo-etching, shown in Figs. 1a and 7a, have any correlation with dislocations (except for association with MPs). This conclusion is based on the comparison of images of the same complex defect revealed by photo-etching and followed by a conventional etch used to decorate dislocations with etch pits (see Fig. 7a, b).

Conclusions

It has been shown that shallow photo-etching in KOH and KOH-KSO aqueous solutions (etch depth less than 100 nm) clearly reveals electrically active non-homogeneities in *n*-type 4H-SiC crystals. Peculiar hexagonal-shaped defects were revealed by etching and examined using Raman spectroscopy. The non-homogeneous distribution of carriers

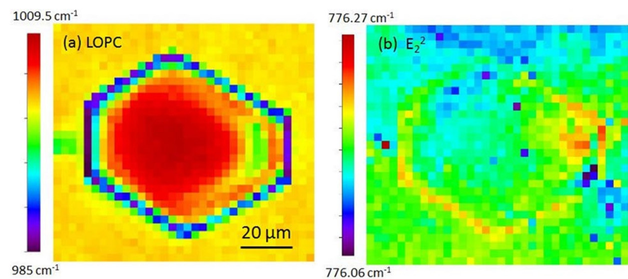

Fig. 9 Raman spectra (μRS-2) were measured at 4-*μ*m intervals over a 132 *μ*m × 120 *μ*m region containing a hexagonal defect in 4H-SiC. Spatial maps are shown for the Raman shift of the (a) LOPC mode and the (b) E_2^2 phonon. The Raman shift of the LOPC increases with increasing free carrier concentration. The Raman shift of the E_2^2 phonon shifts with stress.

across these defects and across growth striations was compared with the photo-etch rate and the quantitative relationship $R = \mathrm{f}\log(n)$ was established. This relationship follows the general rule previously established for other III–V semiconductors. No correlation was found between the hexagonal defects and the dislocations.

Supplementary Information The online version contains supplementary material available at https://doi.org/10.1007/s11664-023-10272-6.

Acknowledgments This work was supported by the Office of Naval Research.

Conflict of interest The authors declare that they have no conflict of interest.

Open Access This article is licensed under a Creative Commons Attribution 4.0 International License, which permits use, sharing, adaptation, distribution and reproduction in any medium or format, as long as you give appropriate credit to the original author(s) and the source, provide a link to the Creative Commons licence, and indicate if changes were made. The images or other third party material in this article are included in the article's Creative Commons licence, unless indicated otherwise in a credit line to the material. If material is not included in the article's Creative Commons licence and your intended use is not permitted by statutory regulation or exceeds the permitted use, you will need to obtain permission directly from the copyright holder. To view a copy of this licence, visit http://creativecommons.org/licenses/by/4.0/.

References

1. M. Katsuno, N. Ohtani, T. Aigo, T. Fujimoto, H. Tsuge, H. Yashiro, and M. Kanaya, Structural properties of subgrain boundaries in bulk SiC crystals. *J. Cryst. Growth* 216, 256 (2000).
2. M. Syväjärvi, R. Yakimova, and E. Janzén, Anisotropic etching of SiC. *J. Electrochem. Soc.* 147(9), 3519 (2000).
3. E. Polychroniadis, M. Syväjärvi, R. Yakimova, and J. Stoemenos, Microstructural characterization of very thick freestanding 3C-SiC wafers. *J. Cryst. Growth* 263, 68 (2004).
4. S. Ha, H.J. Chung, N.T. Nuhfer, and M. Skowronski, Dislocation nucleation in 4H silicon carbide epitaxy. *J. Cryst. Growth* 262, 130 (2004).
5. M. Benamara, X. Zhang, M. Skowronski, P. Ruterana, G. Nonet, J.J. Sumakeris, M.J. Paisley, and M.J. O'Loughlin, Structure of the carrot defect in 4H-SiC epitaxial layers. *Appl. Phys. Lett.* 86, 021905 (2005).
6. T. Hatakeyama, K. Ichinoseki, H. Yamaguchi, N. Sugiyama, and H. Matsuhata, Correlation between surface morphological defects and crystallographic defects. *Mater. Sci. Forum* 717–720, 359 (2012).
7. T. Mitani, M. Okamura, T. Takahashi, N. Komatsu, T. Kato, and H. Okumura, Control of void formation in 4H-SiC solution growth. *Mater. Sci. Forum* 717–720, 57 (2012).
8. H. Fujiwara, T. Kimoto, T. Tojo, and H. Matsunami, Characterization of in-grown stacking faults in 4H–SiC (0001) epitaxial layers and its impacts on high-voltage Schottky barrier diodes. *Appl. Phys. Lett.* 87, 051912 (2005).
9. B. Chen, J. Chen, T. Sekiguchi, T. Ohyanagi, H. Matsuhata, A. Kinoshita, H. Okumura, and F. Fabbri, Electrical activities of stacking faults and partial dislocations in 4H-SiC homoepitaxial films. *Superlattices Microstruct.* 45, 295 (2009).
10. S.I. Maximenko, J.A. Freitas Jr., R.L. Myers-Ward, K.-K. Lew, B.L. VanMil, C.R. Eddy Jr., D.K. Gaskill, P.G. Muzykov, and T.S. Sudarshan, Effect of threading screw and edge dislocations on transport properties of 4H-SiC homoepitaxial layers. *J. Appl. Phys.* 108, 013708 (2010).
11. G. Feng, J. Suda, and T. Kimoto, Nonradiative recombination at threading dislocations in 4H-SiC epilayers studied by micro-photoluminescence mapping. *J. Appl. Phys.* 110, 033525 (2011).
12. Wu. Ping, Etching study of dislocations in heavily nitrogen doped SiC crystals. *J. Cryst. Growth* 312, 1193 (2010).
13. H. Song, T. Rana, and T.S. Sudarshan, Investigations of defect evolution and basal plane dislocation elimination in CVD epitaxial growth of silicon carbide on eutectic etched epilayers. *J. Cryst. Growth* 320, 95 (2011).
14. R. Han, B. Han, D.H. Wang, and C. Li, Temperature dependence of Raman scattering from 4H-SiC with hexagonal defects. *Appl. Phys. Lett.* 99, 011912 (2011).
15. J.D. Caldwell, L. Lombez, A. Delamarre, J.-F. Huillemoles, B. Bourgoin, B.A. Hull, and M. Verhaegen, Luminescence imaging of extended defects in SiC via hyperspectral imaging. *Mater. Sci. Forum* 717–720, 403 (2012).
16. J.L. Weyher, S. Lazar, J. Borysiuk, and J. Pernot, Defect-selective etching of SiC. *Phys. Status. Solid.* 4(578), 578 (2005).
17. D.H. van Dorp, J.L. Weyher, and J.J. Kelly, Anodic etching of SiC in alkaline solutions. *J. Micromech. Microeng.* 17, S50–S55 (2007).
18. J.L. Weyher, in: *Handbook on Semiconductors, Completely Revised Edition*, Ed. by T.S. Moss, Vol. 3: Chapter 11: *Materials, Properties and Preparation*, Ed. S. Mahajan, (Elsevier 1994), Characterization of Semiconductors by Etching pp. 995–1031
19. J.L. Weyher, J.J. Kelly, Chapter G-43, *Defect-selective etching of semiconductors*, Springer Handbook of Crystal Growth, Dhanaraj, Byrappa, Prasad, Dudley (Eds.) (Springer-Verlag Berlin, Heidelberg 2010) pp. 1453–1476
20. C. Frigeri, J.L. Weyher, and L. Zanotti, Study of segregation inhomogeneities in GaAs by means of DSL photoetching and EBIC measurements. *J. Electrochem. Soc.* 136, 262 (1989).
21. R. Lewandowska, J.L. Weyher, J.J. Kelly, L. Konczewicz, and B. Lucznik, The influence of free-carrier concentration on the PEC etching of GaN: a calibration with Raman spectroscopy. *J. Crystal Growth* 307, 298 (2007).
22. J.L. Weyher, C. Frigeri, S. Müller, in: Microprobe characterization of optoelectronic materials, Ed. J, Jimenez, Taylor & Francis, (New York. London, Chapter 8: Selective etching and complementary microprobe techniques (SFM, EBIC), 17 pp. 595–689 (2003)
23. J.L. Weyher, F.D. Tichelaar, D.H. van Dorp, J.J. Kelly, and A. Khachapuridze, The $K_2S_2O_8$–KOH photoetching system for GaN. *J. Cryst. Growth* 312, 2607 (2010).
24. G. Kamler, J.L. Weyher, I. Grzegory, E. Jezierska, and T. Wosinski, Defect-selective etching of GaN in a modified molten bases system. *J. Cryst. Growth* 246, 21 (2002).
25. S. Nakashima and H. Harima, Raman investigation of SiC polytypes. *Phys. Status Solidi (A)* 162, 39 (1997).
26. A. Mooradian and G.B. Wright, Observation of the interaction of plasmons with longitudinal optical phonons in GaAs. *Phys. Rev. Lett.* 16, 999 (1966).
27. J.L. Weyher, D. Van Dorp, and J.J. Kelly, Principles of electroless photoetching of non-uniformly doped GaN: kinetics and defect revealing. *J. Cryst. Growth* 430, 21–27 (2015).
28. H. Wang, F. Wu, S. Byrappa, B. Raghothamachar, M. Dudley, P. Wu, I. Zwieback, A. Souzis, G. Ruland, and T. Anderson, Synchrotron topography studies of the operation of double-ended frank-read partial dislocation sources in 4H-SiC. *J. Cryst. Growth* 401, 423–430 (2014).

29. N. Ohtani, M. Katsuno, T. Fujimoto, T. Aigo, and H. Yashiro, Surface step model for micropipe formation in SiC. *J. Cryst. Growth* 226, 254–260 (2001).
30. J. Giocondi, G.S. Rohrer, M. Skoronski, V. Balakrishna, G. Augustine, H.M. Hobgood, and R.H. Hopkins, An atomic force microscopy study of super-dislocation/micropipe complexes on the 6H-SiC(0 0 0 1) growth surface. *J. Cryst. Growth* 181, 351–362 (1997).
31. R.R. Ciechonski, M. Syväjärvi, J.U. Hassan, and R. Yakimova, Structural instabilities in growth of SiC crystals. *J. Cryst. Growth* 275, e461–e466 (2005).
32. X. Ma, Superscrew dislocations in silicon carbide: dissociation, aggregation, and formation. *J. Appl. Phys.* 99(6), 063513 (2006).
33. S. Nishino, T. Higashino, T. Tanaka, and J. Saraie, Growth mechanism and defects in SiC prepared by sublimation method. *J. Cryst. Growth* 147, 339–342 (1995).
34. T.A. Kuhr, E.K. Sanchez, M. Skowronski, W.M. Vetter, and M. Dudley, Hexagonal voids and the formation of micropipes during SiC sublimation growth. *J. Appl. Phys.* 89, 4625 (2001).

Publisher's Note Springer Nature remains neutral with regard to jurisdictional claims in published maps and institutional affiliations.